

PCCP

Physical Chemistry Chemical Physics

Accepted Manuscript

This article can be cited before page numbers have been issued, to do this please use: K. Matsumoto, Y. Nakatsukasa, D. Ioka, Z. Pan, S. H. Choi, W. Y. Sohn and K. Katayama, *Phys. Chem. Chem. Phys.*, 2026, DOI: 10.1039/D6CP00521G.



This is an Accepted Manuscript, which has been through the Royal Society of Chemistry peer review process and has been accepted for publication.

Accepted Manuscripts are published online shortly after acceptance, before technical editing, formatting and proof reading. Using this free service, authors can make their results available to the community, in citable form, before we publish the edited article. We will replace this Accepted Manuscript with the edited and formatted Advance Article as soon as it is available.

You can find more information about Accepted Manuscripts in the [Information for Authors](#).

Please note that technical editing may introduce minor changes to the text and/or graphics, which may alter content. The journal's standard [Terms & Conditions](#) and the [Ethical guidelines](#) still apply. In no event shall the Royal Society of Chemistry be held responsible for any errors or omissions in this Accepted Manuscript or any consequences arising from the use of any information it contains.

Spatially Resolved Visualization of Long-Lived Charge Carriers in Al-Doped SrTiO₃ by the Time-Resolved Microscopy

Kana Matsumoto,¹ Yuki Nakatsukasa,¹ Daisuke Ioka,² Zhenhua Pan,² Seung Heon Choi,³ Woon Yong Sohn^{3,4} and Kenji Katayama^{1*}

¹ Department of Applied Chemistry, Chuo University, Tokyo 112-8551, Japan;

² Department of Applied Chemistry, Graduate School of Engineering, University of Hyogo, Himeji, Hyogo 671-2280, Japan;

³ Department of Chemistry, Chungbuk National University, Cheongju, Chungbuk, Korea

⁴ Chungbuk National University G-LAMP Project Group, Cheongju, Chungbuk, Korea

*Corresponding authors:

K. Katayama, Phone: +81-3-3817-1913, E-mail: kkata.33g@g.chuo-u.ac.jp

Abstract

Al-doped SrTiO₃ (SrTiO₃:Al) exhibits exceptional performance for photocatalytic overall water splitting, yet the microscopic origins of its long-lived charge carriers remain insufficiently understood. Patterned-illumination time-resolved phase microscopy (PI-PM) was applied to directly visualize the spatiotemporal dynamics of electrons and holes in SrTiO₃, SrTiO₃:Al, and Rh-loaded SrTiO₃:Al thin films. PI-PM revealed that Al doping suppresses fast electron–hole recombination pathways associated with Ti³⁺ defect states and introduces a new hole-trapping state with a markedly delayed decay extending over two orders of magnitude compared with pristine SrTiO₃. Clustering analysis of all the local responses distinguished multiple kinetic categories and demonstrated that this Al-induced hole population is selectively quenched by hole scavengers, confirming its assignment as a long-lived, reactive hole species. Rh deposition introduced an additional slower electron response, attributed to electron trapping at Rh cocatalyst sites. Kinetic simulations reproduced these experimental features only when deep Al-induced hole traps and Rh-induced electron traps were incorporated. These results establish that Al doping and cocatalyst loading generate spatially heterogeneous trap states that stabilize long-lived carriers at specific surface domains, providing the mechanistic basis for enhanced charge separation and reactivity in SrTiO₃:Al-based photocatalysts.



Introduction

Photocatalytic water splitting using semiconductor materials has long been regarded as a promising strategy for solar-to-hydrogen conversion, providing a direct route to renewable fuel production without CO₂ emissions. Since the pioneering discoveries of UV-responsive oxide photocatalysts, substantial research efforts have been devoted to designing materials that efficiently absorb sunlight, and drive the reduction and oxidation reactions required for overall water splitting.^{1–4} In particulate photocatalytic systems, the performance strongly depends on the spatio-temporal dynamics of photo-excited carriers, including their trapping, diffusion, interfacial transfer, and recombination processes caused by the intrinsic electronic structure.⁵ Understanding these microscopic dynamical processes has become central to improving material design and maximizing solar-to-hydrogen energy conversion.

Among various semiconductor oxides, strontium titanate (SrTiO₃) has emerged as one of the benchmark materials for photocatalytic overall water splitting.⁶ Stoichiometric SrTiO₃ possesses a suitable conduction-band level for hydrogen evolution and exhibits high chemical stability under strongly oxidative conditions. However, its wide band gap (~3.2 eV) limits absorption to the ultraviolet region. Considerable progress has been made by introducing dopants, cocatalysts and surface structure to enhance visible-light absorption and to modulate charge separation pathways.^{7–10} One of the difficulties to understand the behavior is that the working mechanisms are totally different for crystalline and powder samples.¹¹

One of the most remarkable achievements in photocatalysis is the demonstration that Al-doped SrTiO₃ (SrTiO₃:Al) can reach an apparent quantum yield close to 100% under UV irradiation,¹² indicating that nearly every incident photon is successfully converted into reactive charge carriers that participate in the water-splitting reactions. This extraordinary efficiency originates from the suppression of deleterious charge-carrier recombination processes and the enhancement of interfacial kinetics, both of which are strongly influenced by microscopic charge-carrier behavior, and the enhanced performance can be explained by the improved charge-carrier transport properties and the formation of well-defined reaction sites upon cocatalyst loading.^{13,14}

Beyond material-level improvements, the scalability and practicality of particulate water-splitting systems have been demonstrated by the construction of a 100-m² photocatalyst sheet panel,^{15,16} one of which was deployed by SrTiO₃:Al as the hydrogen-evolution photocatalyst.¹⁷ This large-area demonstration underscores the potential of SrTiO₃-based materials for industrial-scale hydrogen production and highlights the importance of understanding and optimizing charge-carrier processes at both microscopic and device levels.

Despite its demonstrated capability to achieve apparent quantum efficiencies approaching unity and support large-area hydrogen-production panels, the fundamental microscopic mechanism

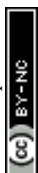


underlying its exceptional activity remains under debate. Recent mechanistic studies have converged on two key roles of SrTiO₃:Al.^{18–20} First, Al doping suppresses native Ti³⁺ donor defects that act as deep electron recombination centers. Surface-sensitive XPS, EPR, and depth-dependent spectroscopic measurements reveal that Ti³⁺ species, widely present on pristine SrTiO₃,^{21–23} are almost completely eliminated upon Al substitution at Ti sites.^{24–27} This defect suppression slows band-to-band electron–hole recombination, thereby extending the effective carrier lifetime. This phenomenon has been confirmed in ultrafast spectroscopy and kinetic modeling studies, which show that the recombination rate in SrTiO₃:Al is reduced by orders of magnitude.

Second, Al doping introduces structural distortions—principally through the formation of AlO₆ units that substitute TiO₆—that generate new hole trapping states and modulate the local polarizability of the TiO₆ lattice.²⁵ Transient absorption spectroscopy shows signatures of hole trapping induced by Al substitution, accompanied by prolonged hole lifetimes extending into the millisecond–second domain.²⁶ Such long-lived holes are essential for driving the intrinsically slow oxygen-evolution reaction in particulate photocatalysts. These findings are reinforced by photoinduced absorption and diffuse reflectance transient spectroscopy, where Al-doped SrTiO₃ consistently exhibits a larger amplitude of hole accumulation and markedly slower decay components than undoped SrTiO₃.²⁴ The combination of defect suppression and long-lived hole stabilization enables charge separation to outcompete recombination and is now recognized as a central mechanistic feature giving rise to the high efficiency of Al-doped SrTiO₃.

Although conventional spectroscopic methods, while powerful for ensemble-averaged kinetic analysis, cannot directly reveal where electrons and holes accumulate in particulate ensemble, how these trapped carriers are spatially distributed, or which microscopic regions contribute to reactive versus non-reactive pathways. Therefore, a microscopic method capable of directly visualizing the spatial distribution of electron and hole dynamics is needed to fully understand where and how charge carriers survive, accumulate, or recombine across the SrTiO₃:Al surface. In this work, we apply our pattern-illumination time-resolved phase microscopy (PI-PM) technique to resolve the local charge-carrier behavior with microscopic spatial and nanosecond temporal resolution and to clarify the microscopic origins of Al-induced efficiency enhancement.

The PI-PM method, which is uniquely capable of visualizing the local charge carrier dynamics with high spatial and temporal precision. PI-PM detects refractive-index changes originating from non-radiative trapped electrons and holes, enabling the separate observation of long-lived electron and hole populations. Moreover, by coupling PI-PM data with clustering analysis, the spatio-temporal heterogeneity of carrier dynamics—arising from variations in defects, facets, or cocatalyst distributions—can be quantitatively mapped. This method has already succeeded in clarifying charge-carrier inhomogeneity and interfacial transfer in perovskites,^{28,29} TiO₂,^{30,31} BiVO₄,^{32,33} oxysulfides,³⁴ and photocatalyst sheets,³⁵ indicating this method applicable for studying the SrTiO₃:Al surface.



Through this approach, we aim to reveal how localized trapping manifest at specific microscopic domains, thereby providing the missing spatial dimension required to fully understand how Al doping modifies trapping pathways, how cocatalysts modulate interfacial transfer, and how microscopic inhomogeneity governs the overall reaction performance.

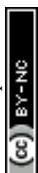
Experimental

PI-PM method

The PI-PM method was employed to visualize the spatiotemporal behavior of photo-excited charge carriers. The fundamental principles, optical configuration, and analytical framework of PI-PM have been described in detail in our previous reports and review articles.³⁶ Briefly, PI-PM is a pump–probe phase-contrast microscopy technique in which both pump and probe beams are collimated to shine the sample surface, and the phase-contrast image is obtained by the wide-field imaging. A transient refractive index change induced by the photo-excited charge carriers is imaged by intentionally shifting the focus position to enhance phase contrast.³⁷ Because the refractive-index-based detection is sensitive to the generation and decay of the surface and defect-trapped carriers after the free carrier decay and this information is complimentary to the charge carrier dynamics obtained by the transient absorption or photoluminescence techniques, where the free carrier decay is generally observed.

Both pump and probe beams were nanosecond pulsed Nd:YAG lasers (pulse width 3–4 ns). The probe delay was controlled electronically to obtain a time-resolved image sequence following pump excitation. Arbitrary spatial patterns were projected onto the sample using a digital micromirror device (DMD), enabling spatially selective carrier excitation. Photo-excited carriers subsequently undergo trapping, recombination, interfacial transfer, and diffusion, and the resulting refractive-index variation is recorded as a phase-contrast image sequence. Such patterned excitation is essential for extracting pump–probe contrast and to ensure stable reconstruction of the spatiotemporal carrier distribution in the following image recovery technique. Because pulsed-laser imaging introduces strong spatial and temporal intensity fluctuations, the acquired image stacks were processed using three-dimensional total-variation (3D-TV) regularization (x, y, t dimensions) to suppress noise while preserving structural features.³⁸ This denoising strategy, established in our earlier PI-PM studies enables quantitative analysis of local carrier dynamics in heterogeneous photocatalytic and photovoltaic materials. After the image quality improvement, pixel-wise temporal traces (>10000 traces) were used for analyses such as carrier-type classification by the clustering technique, a methodology that has proven effective for separating electron and hole processes as well as identifying domain-dependent dynamics.

In this study, a horizontally aligned striped pattern was used as the pump illumination. The patterned region was centered on the field of view, yielding an imaging area of $480.8 \times 93.9 \mu\text{m}$ (1024×200 pixels; pixel size 469 nm). The third harmonic of a Nd:YAG laser (355 nm, 3 ns pulse width,



GAIA, Rayture Systems) served as the pump (0.8 mJ/pulse), and the second harmonic of another Nd:YAG laser (532 nm, 0.02 mJ/pulse) was used as the probe. The pump-irradiated region had a diameter of 0.5 mm. The phase-contrast microscope provided a lateral resolution of 2–3 μm . Although the optical setup can detect both refractive-index and absorption changes, the absorption change was negligible for SrTiO₃ at 532 nm under the wide-field detection, as confirmed by measurements performed at the exact focal plane, where refractive-index change diminishes. The complete optical layout is shown in **Error! Reference source not found.** in Supporting Information (SI).

Clustering analysis

In the PI-PM analysis, the classification of surface charge carrier types was performed using clustering analysis. A specific region (30 \times 50 μm) within the pump-illuminated area was selected, containing more than 10,000 pixel-wise temporal response curves. Each curve consisted of approximately 100–200 time-resolved signal intensities spanning from nanoseconds to milliseconds. These responses were treated as numerical vectors and categorized according to their waveform similarity using spectral clustering, a statistical classification technique based on similarity metrics.³⁹ In this procedure, the similarity between vectors was evaluated using normalized correlation matrices, enabling the grouping of signals that exhibit analogous temporal characteristics. The resulting clusters were then refined through manual inspection to remove irregular or anomalous traces, which were labeled as outliers. Finally, the categorized responses were mapped back onto the optical image, yielding a spatial distribution of the cluster types and thereby visualizing the local variation in charge carrier behavior across the sample surface.

Sign of refractive index change

When the probe wavelength (532 nm) is longer than the band-edge absorption of the material, changes in optical absorption contribute only minimally to the detected signal. Under these conditions, PI-PM predominantly captures refractive-index changes associated with trapped charge carriers at interfaces.³⁶ The accumulation of charges at an interface generates a local electric field, E_{local} , which can be expressed as

$$E_{local} = \frac{\sigma}{\epsilon_r \epsilon_0}, \quad (1)$$

where σ is the surface charge density (positive for holes and negative for electrons), ϵ_r is the relative permittivity, and ϵ_0 is the vacuum permittivity. The sign of σ determines the direction of E_{local} and consequently whether electrons or holes accumulate at the interface. This local electric field alters the material permittivity through the linear electro-optic (Pockels) effect. The corresponding change in permittivity is

$$\Delta\epsilon = -\epsilon_r^2 r E_{local}, \quad (2)$$

where r is the Pockels coefficient. An interfacial electric field produced by holes ($\sigma > 0$) increases the



permittivity, while that produced by electrons ($\sigma < 0$) decreases it. Physically, electrons draw the electric field toward the interface, reducing the permittivity and inducing a phase advance in the transmitted light, with the opposite effect occurring for holes.

The refractive-index change detected by PI-PM is related to the permittivity change by

$$\Delta n \cong \frac{\Delta \epsilon}{2n}, \quad (3)$$

derived from the approximation $(n + \Delta n) \cong (\epsilon + \Delta \epsilon)^{1/2}$ for small perturbations. This relationship indicates that electrons and holes induce refractive-index changes of opposite sign in the same material. Consequently, PI-PM can distinguish between electron- and hole-dominated responses based solely on the sign of Δn , providing a powerful means of identifying charge carrier type in heterogeneous photocatalytic and photovoltaic materials.

Sample preparation

Preparation of SrTiO₃.

Strontium titanate (SrTiO₃) powder was synthesized by a conventional solid-state reaction.^{40,41} Stoichiometric amounts of SrCO₃ and TiO₂ were mixed at a molar ratio of 1.03:1, followed by calcination at 1150 °C for 10 h in air to obtain crystalline SrTiO₃. The resulting powder (0.01 g) was dispersed in 1000 μL of isopropanol and subjected to sonication for 10 min to achieve uniform particle dispersion. A thin-film substrate was prepared by drop-casting 40 μL of this dispersion five times onto a clean glass slide and allowing it to dry naturally in air.

Preparation of Al-doped SrTiO₃ (SrTiO₃:Al).

Al-doped SrTiO₃ was prepared via a flux-assisted solid-state reaction⁴² using SrTiO₃, Al₂O₃, and SrCl₂ in a molar ratio of 1:0.04:10. The mixture was calcined at 1150 °C for 10 h. After cooling, the obtained SrTiO₃:Al powder (0.01 g) was dispersed in 1000 μL of isopropanol and ultrasonicated for 10 min. A thin-film substrate was fabricated by drop-casting 40 μL of the dispersion five times onto a glass slide, followed by natural drying.

Preparation of Rh-loaded SrTiO₃:Al (Rh/SrTiO₃:Al).

The SrTiO₃:Al powder was dispersed in 100 mL of deionized water, to which an aqueous RhCl₃ solution (0.1 wt % Rh) was added under magnetic stirring. The suspension was purged with argon and irradiated with a 300 W Xe lamp (full arc) for 10 min in a closed circulation system to photodeposit Rh. The resulting Rh-loaded SrTiO₃:Al particles were collected by filtration and washed with water.⁴⁰ For film preparation, 0.01 g of Rh/SrTiO₃:Al was dispersed in 1000 μL of isopropanol and sonicated for 10 min, followed by drop-casting 40 μL of the dispersion five times onto a glass slide and air drying.

Measurement Cell

A sample film on a slide glass substrate was sandwiched by another glass substrate with a rubber



spacer (thickness; 0.5 mm). An amount of 0.15 mL of liquid was introduced into the gap layer. Each sample was measured in contact with acetonitrile (ACN), ethanol (EtOH), and a solution of 0.1 mM nitrobenzene in EtOH (NB/EtOH), respectively. ACN was used as an inert solution to prevent charge transfer from the photocatalytic materials to the liquid. EtOH was used as a hole scavenger, while the NB/EtOH served as a scavenger for both electrons and holes. In the previous research,⁴³ it was clarified that NB was reduced and transformed into nitrosobenzene during the photocatalytic process in EtOH.

Results and Discussions

Figure 1 shows the time-resolved image sequences of the refractive-index changes for (a) SrTiO₃, (b) SrTiO₃:Al, and (c) Rh/SrTiO₃:Al thin films measured by the PI-PM method in ACN. The stripe-like contrasts, corresponding to the modulated pump-light pattern, appeared immediately after the UV pump pulse and intensified within 100 ns before decaying within 10–100 μs for all samples. The observed phase contrast originates from the transient refractive-index change induced by photo-excited charge carriers, consistent with the earlier reports on SrTiO₃ single crystals and particulate films,⁴⁴ where the signal rise and decay reflect charge-carrier trapping and recombination processes. The gradual growth of the contrast, for particulate SrTiO₃, suggests the formation of shallowly trapped carriers diffusing between particles before recombination, as previously described⁴⁴ and simulated theoretically.^{34,45} Similar temporal behaviors were also observed in PI-PM measurements of other particulate photocatalysts such as BiVO₄ and SrTiO₃ composites.³⁵ These responses of the refractive-index changes visualized by PI-PM mainly reflect the population and relaxation of trapped charge carriers rather than the free-carrier response.

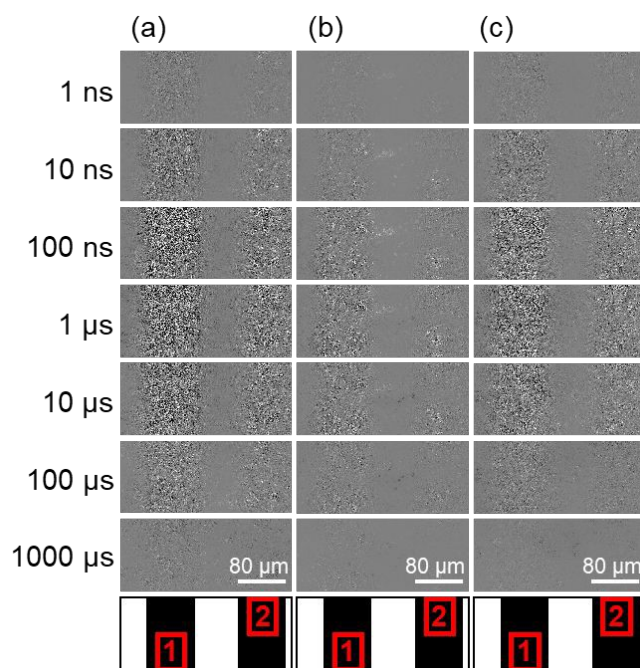


Figure 1 Time-resolved image sequences of the refractive-index change obtained by pattern-illumination time-resolved phase microscopy (PI-PM) for (a) SrTiO₃, (b) Al-doped SrTiO₃ (SrTiO₃:Al), and (c) Rh-loaded SrTiO₃:Al (Rh/SrTiO₃:Al) thin films. Each frame corresponds to a different delay time after photoexcitation by the patterned pump light ($\lambda = 355$ nm). The bright and dark regions represent the positive and negative phase shifts caused by transient refractive-index changes associated with photo-excited charge carriers. The bottom diagram indicates the light intensity pattern (black region corresponds to the irradiated region.), and the red rectangle represents the analyzed regions by the clustering analysis.

We analyzed the local charge carrier dynamics in the light-irradiated regions ($100 \times 50 \mu\text{m}^2$) indicated in **Figure 1a** as the region 1. Following the established analysis protocol described in our previous studies,³⁶ all pixel-by-pixel temporal responses in the region were collected and categorized using spectral clustering, in which the similarity between temporal response vectors was evaluated based on their amplitude and shape. After clustering, each response category was averaged, and the spatial distribution of each type was mapped onto the microscopic image. **Figure 2b–d** show the clustering results for SrTiO₃ in ACN, EtOH, and NB/EtOH, respectively. Two distinct categories of responses were observed in ACN: a positive rise-and-decay response with time constants of rise = 15 ± 1 ns and decay = 22 ± 2 μs (green), and a negative valley-and-recovery response with fall = 17 ± 1 ns and recovery = 15 ± 1 μs (yellow). The opposite signs of the refractive-index change indicate different carrier types, electrons and holes, respectively, as previously reported for particulate SrTiO₃ and TiO₂ films.⁴⁴

By introducing the hole scavenger EtOH, the yellow-region area decreased, confirming its attribution to hole dynamics. Conversely, in a solution including electron scavenger, (NB/EtOH), the green-region signal was suppressed, verifying that the positive (green) response corresponds to the electron signal. The region 2 result is presented in **Error! Reference source not found.** in SI, and the similar tendency was observed. These observations are consistent with earlier reports that the sign of the PI-PM phase response to electron and hole dynamics at the interface. Notably, the scavenger effects in SrTiO₃ were relatively small compared with those observed for Fe₂O₃ and BiVO₄,⁴⁶ implying limited interfacial hole transfer in pristine SrTiO₃.



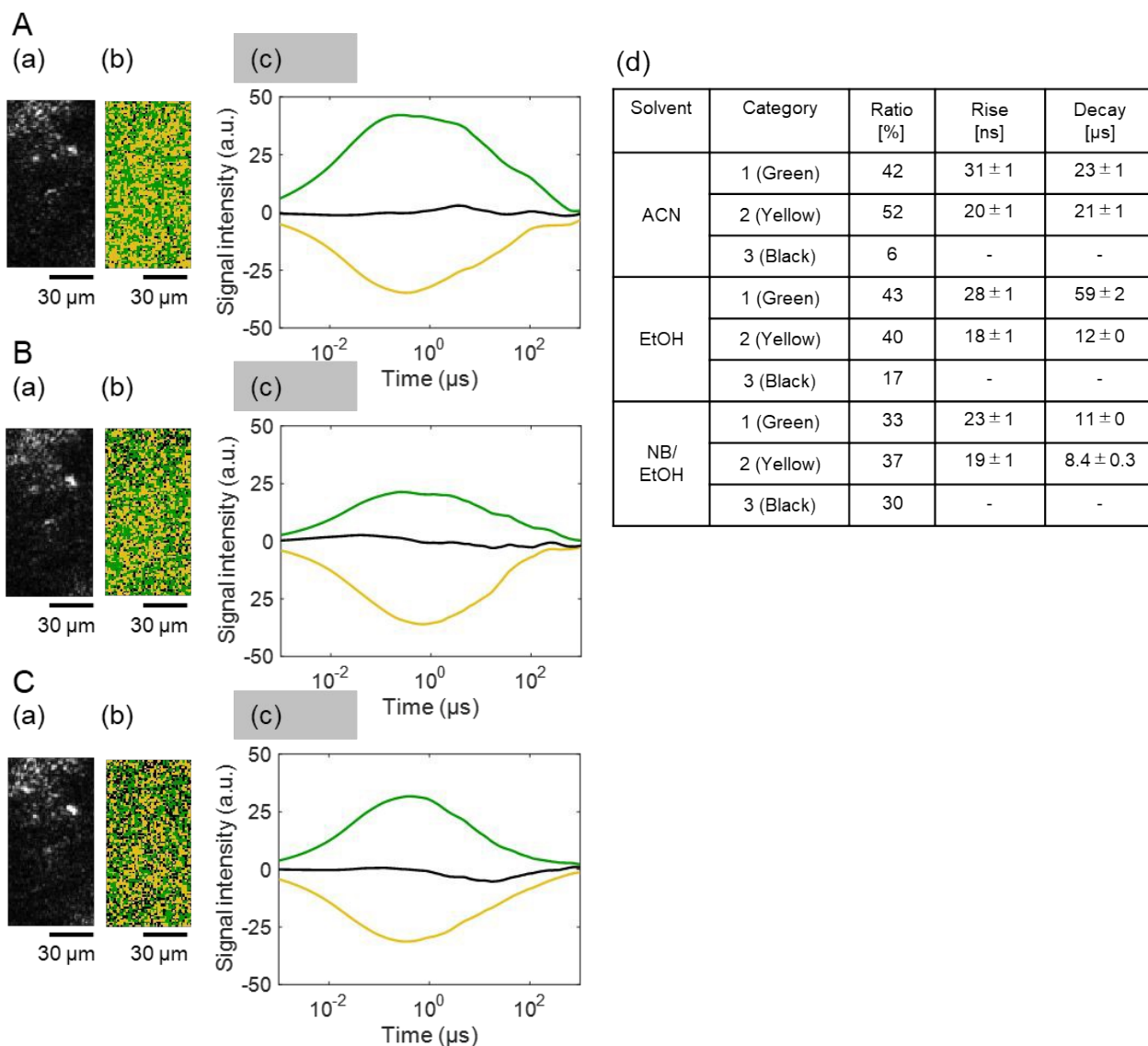
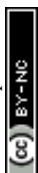


Figure 2 The clustering analyses of the charge carrier responses of a pristine SrTiO₃ in (A) ACN, (B) EtOH, and (C) NB/EtOH in Region 1 in **Figure 1(a)**. (a) correspond to a microscopic image, and the corresponding categorized map is shown in (b), and the scale bar corresponds to 30 μ m. The averaged responses for the categorized responses are shown in (c). The area ratios of categories and the rise/decay times for the categories are shown in (d).

Next, we analyzed the local charge carrier dynamics in the illuminated region ($100 \times 50 \mu\text{m}^2$) indicated in **Figure 1(b)** for the SrTiO₃:Al thin film. As in the case of pristine SrTiO₃, all pixel-by-pixel temporal responses were collected and categorized by the spectral-clustering procedure based on the similarity of their amplitude vectors. From this analysis, positive and negative refractive-index changes were again observed; however, the negative responses were separated into two distinct



categories with different temporal constants. The positive signal (green) exhibited a rise-and-decay response (rise = 57 ± 2 ns and decay = 46 ± 2 μ s (green)) assigned to electrons, while the two negative signals (yellow and magenta) corresponded to holes with faster and slower kinetics (fall = 12 ± 0 ns and recovery = 2.1 ± 0.1 μ s (yellow), fall = 301 ± 11 ns and recovery = 119 ± 4 μ s (magenta), respectively).

In the EtOH solution, used as a hole scavenger, only the slower negative component (magenta) was reduced in the mapped region, whereas the faster negative and positive components remained unchanged. This selective suppression indicates that the slower magenta response originates from reactive hole dynamics participating in surface oxidation. Conversely, in the NB/EtOH solution, which scavenges electrons, the positive (green) response was effectively diminished, confirming its assignment to electrons. The result for region 2 is displayed in **Error! Reference source not found.** in SI, and a similar tendency was confirmed.

The slower hole response (magenta) showed markedly delayed kinetics compared with the responses observed for pristine SrTiO₃: the fall and recovery components were both retarded, and the decay constant extended from approximately 2.1 μ s to 119 μ s. Moreover, the temporal peak position of this component shifted by about two orders of magnitude (from 10^{-1} μ s to 10^1 μ s) relative to the undoped sample. These findings indicate that Al doping introduces an additional hole-trapping state, which stabilizes photogenerated holes and prolongs their lifetime. More than a half of the yellow region was converted into the magenta region in the spatial map also suggests enhanced hole accumulation near the surface due to the modification of local structure by Al substitution.

Such prolonged hole lifetimes are consistent with the emergence of shallow acceptor-like states associated with Al dopants, which slow recombination and facilitate oxidative reactions on the surface. Therefore, Al doping effectively creates an additional, longer-lived hole population that is more chemically reactive, leading to improved oxidation efficiency in photocatalytic processes. These microscopic observations of carrier dynamics directly visualize how Al incorporation alters the trapping distribution and extends the lifetime of holes in SrTiO₃-based photocatalysts.



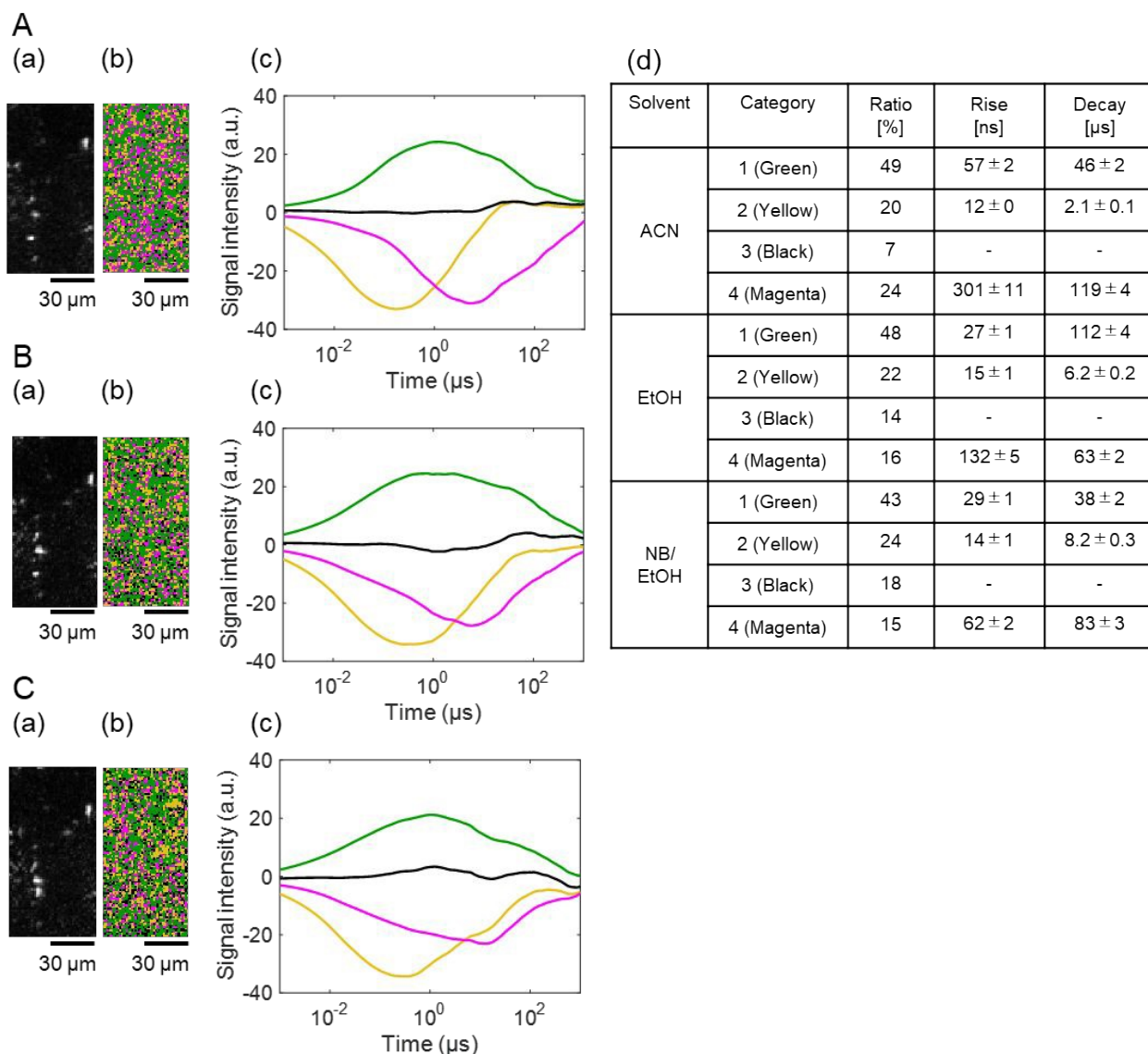


Figure 3 The clustering analyses of the charge carrier responses of a Al-doped SrTiO_3 ($\text{SrTiO}_3:\text{Al}$) in (A) ACN, (B) EtOH, and (C) NB/EtOH in Region 1 in **Figure 1(b)**. (a) correspond to a microscopic image, and the corresponding categorized map is shown in (b), and the scale bar corresponds to 30 μm . The averaged responses for the categorized responses are shown in (c). The area ratios of categories and the rise/decay times for the categories are shown in (d).

The local charge carrier dynamics of the Rh-loaded $\text{SrTiO}_3:\text{Al}$ ($\text{Rh}/\text{SrTiO}_3:\text{Al}$) thin film were analyzed in the light-irradiated region ($100 \times 50 \mu\text{m}^2$) indicated in **Figure 1(c)**. The pixel-by-pixel temporal responses were categorized by spectral clustering as described previously. Three representative categories of responses were observed (green, yellow, and magenta), which correspond to the same types of charge carriers identified in the undoped and $\text{SrTiO}_3:\text{Al}$ samples. In addition to



these, a newly delayed positive response (blue) appeared upon Rh loading. From its positive refractive-index sign and the disappearance of this response by the electron scavenger (NB), this delayed response is assigned to an additional electron-trapping process introduced by the Rh cocatalyst.

The hole-scavenging experiments by ethanol yielded results similar to those of SrTiO₃:Al; the slower negative response (magenta) decreased in area, while the faster hole response (yellow) was little affected. In contrast, when NB was added as an electron scavenger, the area corresponding to the delayed positive response (blue) decreased markedly, whereas the green component remained unchanged. The result for region 2 is displayed in **Error! Reference source not found.** in SI, and showed a similar tendency. These observations confirm that the Rh cocatalyst forms electron sites that capture photogenerated electrons and retard their recombination. The delayed electron response thus originates from the charge carriers captured at the Rh cocatalyst.

Such long-lived electron-trapping behavior induced by Rh loading is consistent with previous PI-PM analyses of Rh-loaded La₅Ti₂Cu_{0.9}Ag_{0.1}O₇S₅³⁴ and CoPi-modified hematite films,³¹ in which cocatalyst sites acted as electron or hole reservoirs prolonging carrier lifetimes and facilitating surface redox reactions, and also for SrTiO₃ by the transient absorption method.^{47,48} The extension of the electron lifetime observed here implies more efficient accumulation of reduction-active carriers on the Rh sites, thereby enhancing the overall photocatalytic reduction reactivity. Consequently, the Rh cocatalyst not only provides active surface sites for the reaction but also serves as an electron storage center that suppresses recombination and stabilizes photogenerated charge carriers in SrTiO₃:Al.



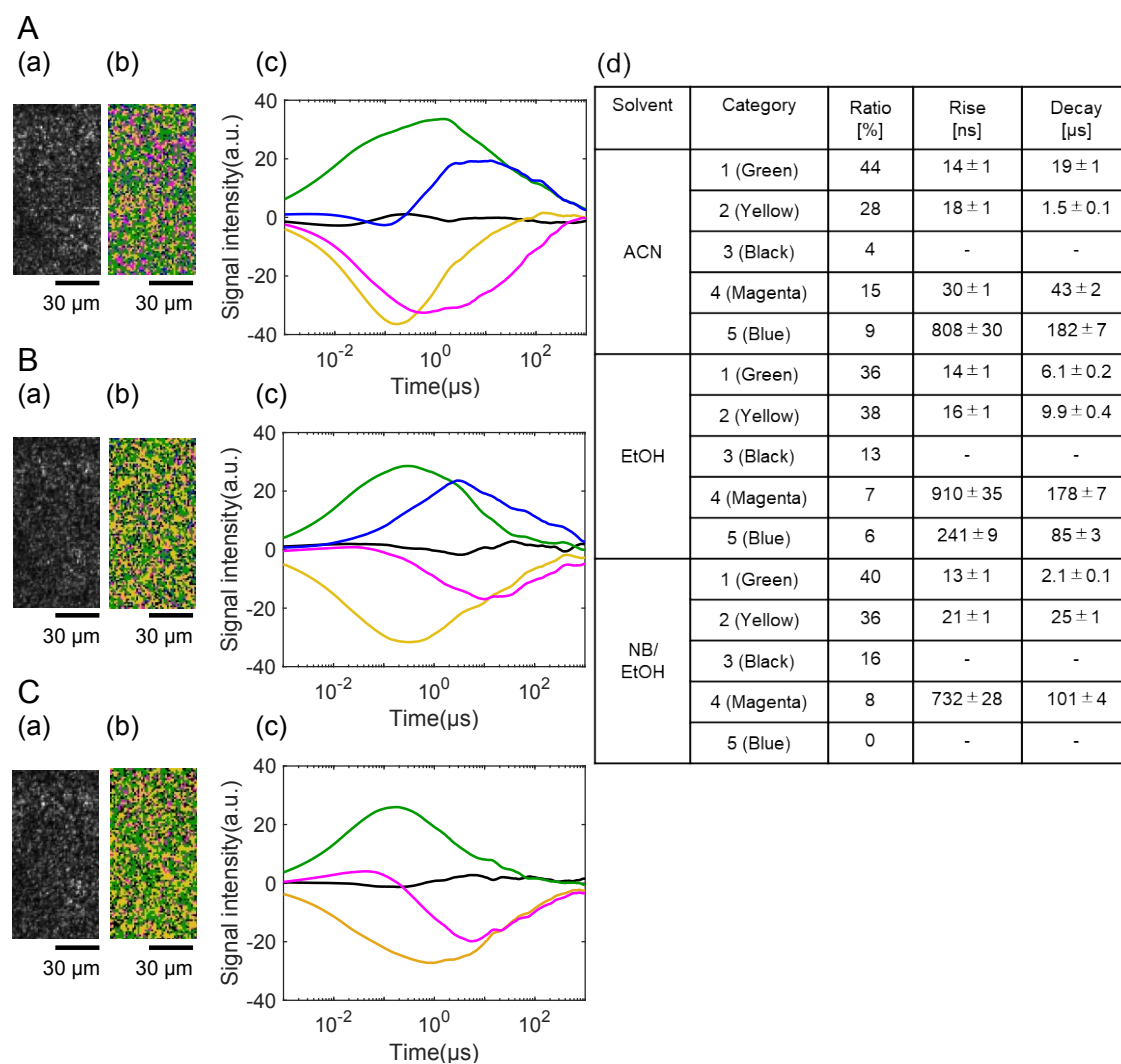


Figure 4 The clustering analyses of the charge carrier responses of a Rh/SrTiO₃:Al film in (A) ACN, (B) EtOH, and (C) NB/EtOH in Region 1 in **Figure 1(c)**. (a) correspond to a microscopic image, and the corresponding categorized map is shown in (b), and the scale bar corresponds to 30 μ m. The averaged responses for the categorized responses are shown in (c). The area ratios of categories and the rise/decay times for the categories are shown in (d).

To further elucidate the origins of the different transient responses observed for SrTiO₃, SrTiO₃:Al, and Rh/SrTiO₃:Al, numerical simulations of charge-carrier kinetics were performed based on rate-equation models incorporating photoexcitation, trapping, detrapping, and recombination processes (see SI, Simulation procedure for charge carrier kinetics for details). In this model, photoexcited free electrons and holes in the conduction and valence bands ($n_m(t)$ and $p_m(t)$) are dynamically exchanged with their respective trap states ($n_t(t)$, $p_t(t)$) through thermally activated



trapping and detrapping steps. The refractive-index variation measured by PI-PM is primarily governed by the population changes in the trapped states, because the signal rise and decay occur on the nanosecond-to-microsecond timescales corresponding to trap-population dynamics rather than direct free-carrier responses.

For pristine SrTiO₃, the model assumed one electron-trap and one hole-trap state located approximately 30 meV below the conduction band and above the valence band, respectively (**Figure 5a**). The simulation reproduced the experimental rise (~10–20 ns) and decay (~1 μs) behaviors by setting trapping and recombination rate constants on the order of 10⁷ and 10⁶ s⁻¹, respectively, confirming that the observed PI-PM response mainly reflects the equilibrium and recombination of shallowly trapped carriers. It is noted that the positions of the trap-state energy levels and the corresponding trap rates compensate each other for the decay/recovery times, and we could not exclusively determine the absolute values of them, and we could only provide the rough estimates of them and check if the numerical model could successfully recover the response shapes.

In SrTiO₃:Al, an additional hole-trapping state above the valence band was introduced to account for the newly observed slower magenta response (**Figure 5b**). The reduced trapping rate (1-2 orders) reproduced the experimentally observed delayed rise and long decay (tens of microseconds). This shallower hole-trapping site, likely associated with Al substitution and neighboring oxygen vacancies, stabilizes photogenerated holes and extends their lifetime, consistent with the enhanced oxidative reactivity observed experimentally.

For Rh/SrTiO₃:Al, an additional electron-trapping state below the conduction band was incorporated to model the newly appearing delayed positive (blue) response (**Figure 5c**). The Rh-related capture exhibited a slower trapping rate than that of the intrinsic trap, resulting in microsecond-scale electron accumulation. Because the Rh state functions as a nonrecombining electron reservoir, this delayed component corresponds to the long-lived electrons localized at the Rh cocatalyst surface, which enhances interfacial reduction reactions. These electrons are assumed to decrease by incorporating the equilibrium with the free electrons.

The overall simulation results successfully reproduced the relative timescales, amplitudes, and signs of the experimental PI-PM transients for all three systems, establishing a consistent kinetic framework linking the trap energetics and rate constants to the observed charge-carrier dynamics. All the parameters used for the simulation are described in **Error! Reference source not found.** and **Table S1**.



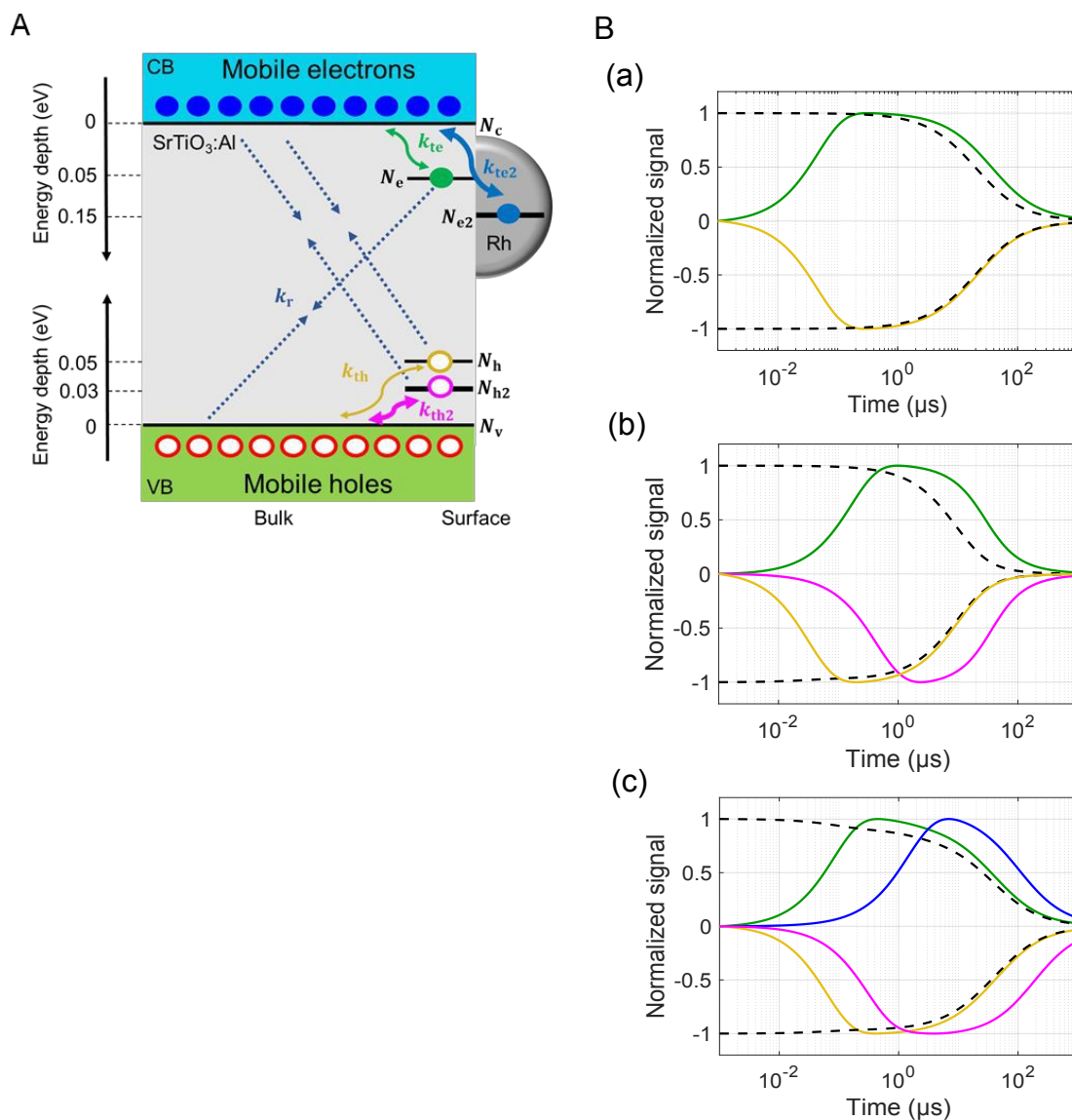
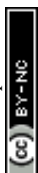


Figure 5 Charge carrier kinetics of the Rh/SrTiO₃:Al photocatalyst. (A) Numerical scheme highlighting the trap and the cocatalyst states, and the recombination channels considered are listed. Here, the effective rate constants for trapping were considered to account for diffusion and charge transfer processes to shallow/deep trap states and/or Rh co-catalyst. (B) Normalized simulated kinetics of mobile (dashed lines) and trapped (solid lines) electrons and holes with time t for different trapping rates and trap states for (a) SrTiO₃, (b) SrTiO₃:Al, (c) Rh/SrTiO₃:Al.

The PI-PM observations and kinetic simulations presented in this work provide direct, real-space evidence that advances the mechanistic consensus established by recent studies on Al-doped



SrTiO₃. As summarized in Introduction, two fundamental aspects have emerged from spectroscopy, surface science, and kinetic analyses of SrTiO₃:Al: (1) suppression of Ti³⁺ defect states, which serve as electron-trapping recombination centers, and (2) formation of new hole-trapping states associated with Al substitution, which prolong hole lifetimes and stabilize oxidative charge carriers.^{24–26} The PI-PM results obtained here are fully consistent with these mechanistic trends while offering previously inaccessible spatial information on the heterogeneity of trap states and the domain-selective dynamics of electrons and holes.

First, PI-PM directly visualized the suppression of hole-recombination pathways as a consequence of Al doping. In pristine SrTiO₃, electrons and holes exhibited symmetric shallow-trap kinetics on nanosecond–microsecond timescales, which matched the simulation model containing only shallow electron and hole traps. In contrast, SrTiO₃:Al showed a clear reduction in the relative population of fast hole–electron recombination signatures and a shift toward a more sustained hole response, consistent with earlier reports of Ti³⁺ defect removal following Al incorporation.^{24,26} The kinetic simulation reproduced this behavior, indicating that the experimentally observed PI-PM response is a direct manifestation of defect suppression.

Second, PI-PM independently identified and spatially resolved the new Al-induced hole-trapping state that has been proposed in transient absorption spectroscopy and DFT analyses.^{25,26} The negative (hole) responses for SrTiO₃:Al separated into two distinct temporal components—a fast μ s-scale response and a delayed component characterized by a much slower fall and recovery—forming the magenta category in the clustering analysis. This slow component was selectively suppressed in the presence of a hole scavenger, confirming its hole origin, and its temporal behavior shifted by two orders of magnitude compared with pristine SrTiO₃. The kinetic simulations reproduced this slow behavior when 1–2 orders slower kinetics to the trap state was incorporated, providing quantitative agreement with Al-induced trapping proposed in earlier mechanistic studies. Thus, PI-PM provides the first direct microscopic confirmation that Al doping generates a new hole-trapping state, stabilizing long-lived oxidative holes at specific surface domains.

Furthermore, PI-PM reveals new insights that were not available from previous ensemble-averaged methods. While transient absorption and XPS studies have inferred the presence of deep hole traps and defect suppression, they could not determine where such states are located on the particle surface or whether all domains behave identically. In contrast, PI-PM spatially mapped the heterogeneous distribution of the slow hole population, revealing domain-dependent variations in the relative contributions of hole dynamics at different trap states, and they were distributed on micron-scale. These findings indicate that Al doping does not modify the entire SrTiO₃ surface uniformly; instead, Al-induced hole stabilization occurs preferentially at certain microscopic regions, likely associated with local variations in Al incorporation, TiO₆ distortion, or oxygen vacancy configurations.

In the Rh-loaded SrTiO₃:Al system, PI-PM further clarified the electron-accumulation



behavior at Rh cocatalyst sites, consistent with earlier transient spectroscopic observations that Rh-clusters extract and accumulate electrons.²⁶ A new delayed positive (blue) component appeared in the PI-PM kinetics only after Rh loading, and its suppression by an electron scavenger verified its assignment as an electron-trapping process. The kinetic simulations reproduced this behavior only when a new trap-state with slow kinetics was added. These results confirm that the Rh cocatalyst functions not merely as a surface reaction site but as an electron reservoir, prolonging charge separation and promoting efficient reduction reactions, which was directly visualized here for the first time with spatiotemporal resolution.

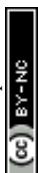
Altogether, the combined PI-PM measurements and kinetic modeling demonstrate that the two accepted mechanistic roles of Al doping— Ti^{3+} defect suppression and the creation of long-lived hole traps—are not only valid but are spatially heterogeneous on the particle surface. PI-PM uniquely visualizes how these processes are distributed across individual grains and how Al- or Rh-induced trap states selectively contribute to carrier lifetime extension.

Conclusion

In this study, we investigated the microscopic charge-carrier dynamics of SrTiO_3 , Al-doped SrTiO_3 , and Rh-loaded $\text{SrTiO}_3:\text{Al}$ by combining patterned-illumination time-resolved phase microscopy (PI-PM) with kinetic modeling. The PI-PM measurements provided spatially resolved visualizations of non-radiative trapped electrons and holes, revealing how Al doping and cocatalyst loading functions charge-carrier pathways at the nanosecond–millisecond scale. Our results directly support the mechanistic roles of Al doping—suppression of Ti^{3+} electron-trapping defects and the creation of new deep hole-trapping states—previously inferred from ensemble spectroscopic studies. PI-PM not only confirmed these processes but also visualized their spatial heterogeneity across the catalyst surface, demonstrating that Al-induced hole stabilization and defect suppression occur preferentially at specific microscopic domains.

The clustering analysis identified distinct temporal categories for trapped electrons and holes and revealed the emergence of a slow, long-lived hole component unique to $\text{SrTiO}_3:\text{Al}$. This slow hole population, selectively quenched by hole scavengers, corresponds to the Al-induced hole state and exhibited a lifetime extended by more than two orders of magnitude compared with pristine SrTiO_3 . Similarly, Rh deposition introduced an additional long-lived electron component, consistent with electron accumulation at Rh cocatalyst sites. These experimentally observed behaviors were reproduced by kinetic simulations only when new trap states were introduced for holes (Al-induced) and electrons (Rh-induced), validating the mechanistic interpretation of the PI-PM responses.

Overall, this work establishes PI-PM as a powerful approach for resolving local charge-carrier dynamics in particulate photocatalysts. By bridging spatially averaged mechanistic models with real-space, domain-specific measurements, we demonstrate that the enhanced photocatalytic



performance of SrTiO₃:Al arises from the presence and distribution of long-lived charge carriers at specific surface domains. These insights highlight the importance of spatial heterogeneity in determining photocatalyst function and provide a foundation for rationally designing next-generation materials by controlling the location, depth, and density of trap states that sustain reactive charge carriers.

Data and Software Availability

All the source analytical data are available on request.

Author Contribution Statement

KM did the experiments and analyses, DI and ZP prepared samples, SC and WS performed analyses and KK guided the overall research. KM and KK wrote the manuscript, and all the authors reviewed it.

Conflict of interests

I declare that the authors have no competing interests or other interests that might be perceived to influence the results and/or discussion reported in this article.

Acknowledgments

The research was financially supported by the Institute of Science and Engineering, Chuo University, Global - Learning & Academic research institution for Master's-PhD students, and Postdocs (LAMP) Program of the National Research Foundation of Korea (NRF) grant funded by the Ministry of Education (No. RS-2024-00445180).

Reference

- 1 S. Chen, T. Takata and K. Domen, *Nature Reviews Materials*, 2017, **2**, 17050.
- 2 Q. Wang and K. Domen, *Chem. Rev.*, 2020, **120**, 919–985.
- 3 Z. Wang, C. Li and K. Domen, *Chem. Soc. Rev.*, 2019, **48**, 2109–2125.
- 4 A. Kudo, Y. Sakata, J. N. Kondo, M. Hara, J. Kubota, S. Ikeda, T. Takata, R. Abe, A. Takagaki and T. Hisatomi, *ACS Catal.*, 2023, **13**, 6934–6955.
- 5 C. Kranz and M. Wächter, *Chem. Soc. Rev.*, DOI:10.1039/D0CS00526F.
- 6 K. Iwashina and A. Kudo, *J. Am. Chem. Soc.*, 2011, **133**, 13272–13275.
- 7 Y. Jia, S. Shen, D. Wang, X. Wang, J. Shi, F. Zhang, H. Han and C. Li, *J. Mater. Chem. A*, 2013, **1**, 7905–7912.
- 8 S. Okunaka, H. Tokudome and R. Abe, *Catal. Sci. Technol.*, 2015, **6**, 254–260.
- 9 S. Okunaka, H. Tokudome and R. Abe, *J. Mater. Chem. A*, 2015, **3**, 14794–14800.



- 10 S. Nishioka, J. Hyodo, J. J. M. Vequizo, S. Yamashita, H. Kumagai, K. Kimoto, A. Yamakata, Y. Yamazaki and K. Maeda, *ACS Catal.*, 2018, **8**, 7190–7200.
- 11 A. Yamakata, J. J. M. Vequizo and M. Kawaguchi, *The Journal of Physical Chemistry C*, 2015, **119**, 1880–1885.
- 12 T. Takata, J. Jiang, Y. Sakata, M. Nakabayashi, N. Shibata, V. Nandal, K. Seki, T. Hisatomi and K. Domen, *Nature*, 2020, **581**, 411–414.
- 13 Y. Ham, T. Hisatomi, Y. Goto, Y. Moriya, Y. Sakata, A. Yamakata, J. Kubota and K. Domen, *J. Mater. Chem. A*, 2016, **4**, 3027–3033.
- 14 L. Tian, X. Guan, Y. Dong, S. Zong, A. Dai, Z. Zhang and L. Guo, *Environmental Chemistry Letters*, 2023, **21**, 1257–1264.
- 15 Y. Goto, T. Hisatomi, Q. Wang, T. Higashi, K. Ishikiriyama, T. Maeda, Y. Sakata, S. Okunaka, H. Tokudome, M. Katayama, S. Akiyama, H. Nishiyama, Y. Inoue, T. Takewaki, T. Setoyama, T. Minegishi, T. Takata, T. Yamada and K. Domen, *Joule*, 2018, **2**, 509–520.
- 16 Q. Wang, S. Okunaka, H. Tokudome, T. Hisatomi, M. Nakabayashi, N. Shibata, T. Yamada and K. Domen, *Joule*, 2018, **2**, 2667–2680.
- 17 H. Nishiyama, T. Yamada, M. Nakabayashi, Y. Maehara, M. Yamaguchi, Y. Kuromiya, H. Tokudome, S. Akiyama, T. Watanabe, R. Narushima, S. Okunaka, N. Shibata, T. Takata, T. Hisatomi and K. Domen, *Nature*, 2021, 1–7.
- 18 Z. Zhao, E. J. Willard, H. Li, Z. Wu, R. H. R. Castro and F. E. Osterloh, DOI:10.1039/C8TA05885G.
- 19 Z. Zhao, R. V. Goncalves, S. K. Barman, E. J. Willard, E. Byle, R. Perry, Z. Wu, M. N. Huda, A. J. Moulé and F. E. Osterloh, DOI:10.1039/C9EE00310J.
- 20 L. L. Rusevich, E. A. Kotomin, G. Zvejnieks, M. M. Kržmanc, S. Gupta, N. Daneu, J. C. S. Wu, Y.-G. Lee and W.-Y. Yu, *J. Phys. Chem. C*, 2022, **126**, 21223–21233.
- 21 Y. Jia, L. Xu, J. Chen, Y. Zeng, Z. Duan, T. Liu and X. Liu, *J. Phys. Chem. C*, DOI:10.1021/acs.jpcc.5c03590.
- 22 A. Zindrou, L. Belles and Y. Deligiannakis, *J. Phys. Chem. C*, 2025, **129**, 15309–15321.
- 23 C. Cheng and R. Long, *J. Phys. Chem. Lett.*, 2021, **12**, 12040–12047.
- 24 D. H. K. Murthy, V. Nandal, A. Furube, K. Seki, R. Katoh, H. Lyu, T. Hisatomi, K. Domen and H. Matsuzaki, *Advanced Energy Materials*, 2023, **13**, 2302064.
- 25 Z. Wei, Y. Zhang, J. Yan, J. Chi, H. Huang, Q. Su, J. Liu and W. Shangguan, *ACS Materials Lett.*, 2024, **6**, 5146–5153.
- 26 A. A. Wilson, B. Moss, A. A. Riaz, C. Kalha, P. K. Thakur, T.-L. Lee, A. Regoutz, T. Takata, T. Hisatomi, K. Domen and J. R. Durrant, *J. Am. Chem. Soc.*, DOI:10.1021/jacs.5c07521.
- 27 T. Takata and K. Domen, *J. Phys. Chem. C*, 2009, **113**, 19386–19388.
- 28 T. Ito and K. Katayama, *ACS Appl. Mater. Interfaces*, 2025, **17**, 26740–26750.



- 29 T. Ito and K. Katayama, *J. Phys. Chem. C*, 2025, **129**, 3136–3144.
- 30 M. Ebihara and K. Katayama, *J. Phys. Chem. C*, 2020, **124**, 23551–23557.
- 31 Y. Egawa, K. Kawaguchi, Z. Pan and K. Katayama, *The Journal of Chemical Physics*, 2024, **160**, 164705.
- 32 Y. Nakatsukasa and K. Katayama, *J. Phys. Chem. C*, 2025, **129**, 18935–18945.
- 33 T. Chugenji, Z. Pan and K. Katayama, *J. Phys. Chem. C*, 2022, **126**, 19319–19326.
- 34 T. Chugenji, Z. Pan, V. Nandal, K. Seki, K. Domen and K. Katayama, *Phys. Chem. Chem. Phys.*, 2022, **24**, 17485–17495.
- 35 M. Ebihara, T. Ikeda, S. Okunaka, H. Tokudome, K. Domen and K. Katayama, *Nat Commun*, 2021, **12**, 3716.
- 36 K. Katayama, *Phys. Chem. Chem. Phys.*, 2024, **26**, 9783–9815.
- 37 K. Katayama, T. Chugenji and K. Kawaguchi, *AIP Advances*, 2021, **11**, 115215.
- 38 X. Huang, J. Fan, L. Li, H. Liu, R. Wu, Y. Wu, L. Wei, H. Mao, A. Lal, P. Xi, L. Tang, Y. Zhang, Y. Liu, S. Tan and L. Chen, *Nature Biotechnology*, 2018, **36**, 451–459.
- 39 U. von Luxburg, *Stat Comput*, 2007, **17**, 395–416.
- 40 Z. Pan, J. J. M. Vequizo, H. Yoshida, J. Li, X. Zheng, C. Chu, Q. Wang, M. Cai, S. Sun, K. Katayama, A. Yamakata and K. Domen, *Angewandte Chemie*, 2025, **137**, e202414628.
- 41 A. Yamakata, H. Yeilin, M. Kawaguchi, T. Hisatomi, J. Kubota, Y. Sakata and K. Domen, *Journal of Photochemistry and Photobiology A: Chemistry*, 2015, **313**, 168–175.
- 42 M. Zhang, P. A. Salvador and G. S. Rohrer, *Journal of the American Ceramic Society*, 2022, **105**, 5336–5346.
- 43 K. Katayama, Y. Takeda, K. Shimaoka, K. Yoshida, R. Shimizu, T. Ishiwata, A. Nakamura, S. Kuwahara, A. Mase, T. Sugita and M. Mori, *Analyst*, 2014, **139**, 1953–1959.
- 44 K. Katayama, T. Chugenji and K. Kawaguchi, *Energies*, 2021, **14**, 7011.
- 45 V. Nandal, R. Shoji, H. Matsuzaki, A. Furube, L. Lin, T. Hisatomi, M. Kaneko, K. Yamashita, K. Domen and K. Seki, *Nat Commun*, 2021, **12**, 7055.
- 46 K. Kawaguchi, T. Chugenji, S. Okunaka, H. Tokudome and K. Katayama, *J. Phys. Chem. C*, 2022, **126**, 6646–6652.
- 47 B. Moss, Q. Wang, K. T. Butler, R. Grau-Crespo, S. Selim, A. Regoutz, T. Hisatomi, R. Godin, D. J. Payne, A. Kafizas, K. Domen, L. Steier and J. R. Durrant, *Nature Materials*, 2021, 1–7.
- 48 Z. Wang, R. Toyoshima, M. Yoshida, K. Mase and H. Kondoh, *J. Phys. Chem. C*, 2024, **128**, 9193–9201.



All the source analytical data are available on request.

Open Access Article. Published on 16 April 2026. Downloaded on 4/17/2026 1:35:55 PM.
This article is licensed under a Creative Commons Attribution-NonCommercial 3.0 Unported Licence.

